Living Planet Fellowship

FINAL REPORT

[Arctic Summer Ice Thickness, Arctic-SummIT]

Dr Jack Landy

University of Bristol, UK

Prepared by	**Jack Landy**
Approved by	**[Coordinator at Host Institution]**
Reference	**ESA Contract No. 4000125582/18/I-NS**
Date of Issue	**yyyy-mm-dd**

1 EXECUTIVE SUMMARY

As the extent of Arctic sea ice has declined at unprecedented speed over the past few decades, we have been able to view only limited snapshots of the ice cover's thickness. Pan-Arctic observations of sea ice thickness have been obtained in recent years by satellite altimeters such as ICESat and CryoSat-2, but conventionally these data are only available during winter months. Standard approaches for processing radar altimeter observations cannot distinguish between the response from ocean water and meltwater pooling at the sea ice surface during summer. Our current understanding of basin-scale sea ice melting patterns during summer are limited to poorly-constrained ice-ocean model simulations, at a time when the ice cover is most dynamic, not to mention biological productivity and ice-ocean geochemical fluxes are most active. Moreover, advanced knowledge of ice conditions – thickness in particular – are critical for managing sustainable commercial enterprises, such as shipping and oil & gas extraction, in the northern polar seas.

In "Arctic-SummIT" we have taken significant steps towards producing the first record of pan-Arctic summer sea ice thickness from CryoSat-2. We have tested multiple processing chains for classifying radar waveform data, de-noising observations, calculating sea ice freeboard, converting to thickness, and validating against reference ice thickness observations. Not all processing options have been successful and obtaining valid sea ice thickness data in the Arctic summer from CryoSat-2 remains a huge challenge. However, we have been able to implement a machine-learning classification algorithm, based on shallow and deep learning strategies, to separate CryoSat-2 echoes from leads and melt pond-covered sea ice. The algorithm has been trained and tested on Sentinel-1 and RADARSAT-2 imagery coinciding with CryoSat-2 orbits, and produces classification accuracies of higher than 80%. We have found that it is critical to classify 'noise' waveforms during summer months too, with noisy observations removed by a chain of filtering algorithms. Sea ice freeboards are calculated for each valid lead estimate and reflect expected pan-Arctic spatial & temporal patterns.

We find that CryoSat-2 sea ice freeboards obtained with our method can reproduce the seasonal evolution of ice melt at the Beaufort Gyre Exploration Program upward looking sonars (ULS) remarkably well, following a simple density conversion to estimate ice draft. However, CryoSat-2 estimates for sea ice thickness typically underestimate coincident airborne EM observations collected by AWI partners over the thickest Central Arctic sea ice. Numerical waveform modelling experiments indicate that CryoSat-2 radar freeboards should be expected to underestimate the true ice freeboard in summer, when the radar signal is tied to melt pond surfaces below the ice mean level. Whilst we have generated a sea ice freeboard product with uncertainties, further work is therefore required to develop a generalized bias correction for the ice freeboard-to-thickness conversion. Thereafter we will be in a position to evaluate year-round sea ice volume fluxes across key Arctic gateways for the period between 2011-2020. Our preliminary work on Arctic-SummIT has contributed to the funding of a large UK NERC grant: PRE-MELT (Preconditioning the trigger for rapid Arctic ice melt) with partners from UCL and NOC.

2 OBJECTIVES AND WORKPLAN

The Arctic-SummIT project team is:

- Jack Landy, University of Bristol, PI
- Geoffrey Dawson, University of Bristol
- Stephen Howell, Environment Canada
- Alex Komarov, Environment Canada
- Thomas Krumpen, AWI
- Michel Tsamados, UCL

Arctic-SummIT was organized by the following two work packages (WPs), addressing Priority Area A of the 2018 Living Planet Fellowship call.

WP1 – A new Arctic summer sea ice thickness product from ESA Cryosat-2

Obj a. Develop an innovative algorithm for separating Cryosat-2 echoes from the ocean versus those from melt-pond covered sea ice and use this to derive sea ice freeboard

Obj b. Validate the Cryosat-2 sea ice freeboard data against coincident airborne or upward-looking sonar ice freeboard/draft observations

Obj c. Generate a new pan-Arctic summer sea ice thickness data product for July-September over the full 2011-2018+ Cryosat-2 record

WP2 – Sea ice volume fluxes for key Arctic gateways from ESA Sentinel-1 and CSA RADARSAT-2

Obj d. Integrate new sea ice volume estimates with ice drift obtained from sequential SAR imagery to monitor the seasonal mass balance of ice through important Arctic Ocean gateways

Timeline:

2018 Q4	Literature review, validation data acquisition, initial testing
2019 Q1	Identify and classify Sentinel-1A&B, RADARSAT-2, Sentinel-2 imagery
2019 Q2	Run, import and analyze GPOD CryoSat-2 L1B 20Hz & 80Hz data
2019 Q3	Manual identification of training ice/ocean samples in imagery
2019 Q4	Develop classification algorithms, estimate sea ice freeboards
2020 Q1	Numerical waveform modelling to characterize freeboard biases
2020 Q2	Test CS2 versus BGEP mooring data and AWI AEM data
2020 Q3	Final product development and reporting

3 WORK PERFORMED

3.1 Scientific context

Sea ice in the Arctic has declined at an unprecedented rate in recent decades (Stroeve, et al., 2012), affecting polar amplification of global warming trends (Serreze, et al., 2009), changes in precipitation (Webster, et al., 2014) and Arctic Ocean freshwater content (Morison, et al., 2012), as well as mid-latitude weather patterns (Overland, et al., 2015). For instance, ice extent in January 2018 was the lowest ever recorded

(NSIDC, 2018). These changes have fostered growing stakeholder interest in the Arctic Ocean, particularly during summer and autumn months when open water area is greatest (Barnhart, et al., 2016), the sea ice is most dynamic (Kwok, et al., 2013) and ocean primary productivity (Arrigo, et al., 2012) and biogeochemical processes (Barber, et al., 2015), are most active. Accurate forecasts of summer sea ice conditions weeks to months in advance would revolutionize polar numerical weather prediction, open the possibility of commercial shipping and cruise ecotourism through the Northern Sea Routes, and improve planning of resource exploitation, fishing and hunting activities in the marginal ice zone (Guemas, et al., 2016).

Our understanding of and ability to predict changes in the Arctic sea ice cover during summer are limited by the availability of remotely-sensed ice observations. Daily measurements of basin-wide sea ice concentration at 10-25 km resolution, obtained from passive microwave radiometers, have been assimilated into ice-ocean modelling systems such as PIOMAS (the Pan-Arctic Ice Ocean Modeling and Assimilation System) (Zhang & Rothrock, 2003). Assimilating ice concentration data has dramatically improved the accuracy of pan-Arctic ice extent predictions for spring and summer (Zhang, et al., 2008) and produced more realistic model distributions of winter ice thickness (Schweiger, et al., 2011). State-of-the-art forecasting systems for short-term sea ice conditions also demonstrate significantly improved fidelity when initialized from winter ice thickness maps (Chen, et al., 2017; Allard, et al., 2018) or sub-model grid ice thickness distributions (Schroeder, et al., 2017). Winter ice thickness observations have generally been derived from satellite laser altimetry (Kwok, et al., 2007), radar altimetry (Laxon, et al., 2013), or L-band radiometry (Kaleschke, et al., 2012).

Despite these promising advances, prognostic models suffer from a complete lack of available ice thickness observations during the Arctic summer. For instance, (Allard, et al., 2018) obtained projections for ice thickness from the Arctic Cap Nowcast/Forecast System (ACNFS) more than twice as close to upward-looking sonar observations between October-April than between May-September, when initialized with winter Cryosat-2 data. (Chen, et al., 2017) demonstrated that improved ice extent forecasts from the NCEP Climate Forecast System, Version 2 (CFSv2), after assimilating winter Cryosat-2 ice thickness, deteriorated rapidly after approximately 3 months. Using a set of idealized model experiments, (Day, et al., 2014) concluded that accurate knowledge of the sea ice thickness field is crucially important for monthly ice extent forecasts, especially in summer.

ESA's SMOS (Soil Moisture and Ocean Salinity) L-band passive microwave radiometer has proven quite successful for monitoring daily ice thickness at 12.5 km resolution within the Arctic marginal ice zone (Kaleschke, et al., 2012). SMOS ice thickness data have been compared with simulated ice thickness from the ECMWF Ocean Reanalysis System 5 (ORAS5), with a view to future data assimilation (Tietsche, et al., 2018). However, the SMOS ice thickness data has several limitations. Most importantly, the penetration depth of the sensor is limited to around 1 m, so that variations in brightness temperature above this limit cannot be related to the fundamental relationship between ice thickness and its emissivity (Tian-Kunze, et al., 2014). Winter ice observations are therefore limited to a maximum thickness of around 1 m, although the penetration depth declines rapidly as a function of bulk ice temperature (Tian-Kunze, et al., 2014), so critically these data are unavailable between April and October.

Radar altimeters do not suffer from this same limitation and the most advanced altimeter to date – Cryosat-2 – employs a synthetic aperture radar capable of measuring centimeter-scale variations in sea ice elevation within kilometer-scale footprints on the ground. Cryosat-2 utilizes delay-Doppler processing to narrow the footprint along-track to only around 300 m and, by taking multiple 'looks' at the surface from a range of angles, reduces speckle interference to enhance measurement precision (Wingham, et al., 2006). Sea ice thickness can be estimated from altimeter observations of the ice freeboard (the portion above sea level) during winter, along with parameterizations for snow & sea ice density and snow depth, using the hydrostatic equation. The ice freeboard is obtained by 'retracking' each altimeter echo to identify the mean sea ice or ocean surface scattering the radar pulse, then subtracting ocean tie-points (i.e. leads) from neighboring sea ice samples (Laxon, et al., 2013). Consequently, accurate separation of radar echoes from leads versus sea ice is a crucial step in the ice thickness processing chain. State-of-the-art classification techniques are based on discriminating between the geometrical shape of the echoes e.g. (Kurtz, et al., 2014; Ricker, et al., 2014; Landy, et al., 2017). For instance, the 'width' or standard deviation of a multilooked waveform stack should be lower from a lead, which is close to a specular reflector for the Ku-band radar around nadir, than from sea ice (Kwok & Cunningham, 2015). The 300-m pulse-Doppler-limited footprint along the track of the satellite increases the probability of a pure reflection from a thin lead, rather than from a mix of ice and ocean (Armitage & Davidson, 2013); providing acceptably reliable freeboard observations. This method has been used by several groups to develop pan-Arctic 5-km maps of sea ice thickness for every winter of the Cryosat-2 record: 2011-2017 (Ricker, et al., 2014; Tilling, et al., 2016).

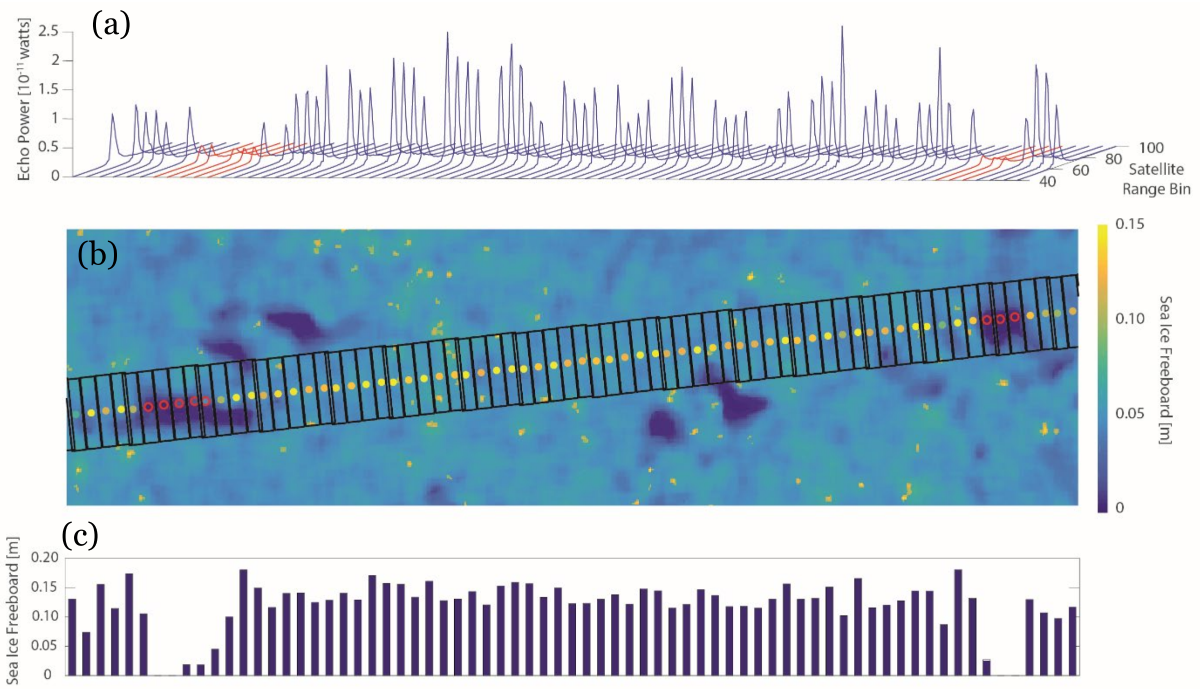

Figure 1 | a. Series of Cryosat-2 SAR echoes, in raw linear uncalibrated power [watts], acquired over sea ice in the Chukchi Sea on 15th July 2017. Echoes with σ^0 (i.e. calibrated backscattered power) below a defined threshold are classified as leads and highlighted in red | **b.** Cryosat-2 footprints (black boxes) along the track of the satellite, with data points at footprint centres illustrating the sea ice freeboard, overlaid on a coincident Sentinel-1b HH-polarized SAR image. Both the Cryosat-2 σ^0 and surface elevation are clearly lower over leads (dark areas) in the Sentinel-1b image. | **c.** Summer sea ice freeboard derived from the Cryosat-2 echoes in a & b, using the new classification scheme and following the technique of (Landy, et al., 2017).

Nevertheless, these conventional techniques cannot reliably be used to separate ice from leads during the Arctic summer. At the onset of summer, snow meltwater pools at the surface of sea ice floes (Landy, et al., 2015), forming melt ponds which lead to strong specular scattering of the radar, just as the leads do (Scharien, et al., 2014). Note, for instance, that most of the echoes from melting sea ice in Figure 1a are sharply-peaked. In our previous example, the standard deviation of the multilooked waveform stack would be low (and indistinguishable) for both leads and melt pond-covered sea ice. It is equally difficult to contrast other geometrical characteristics of ice and lead waveforms, including the commonly-used 'pulse-peakiness' parameter (Kurtz, et al., 2014). Cryosat-2 data have been acquired in SAR and (interferometric) SARIn modes over the Arctic and surrounding oceans during summer months over the entire lifetime of the satellite; but conventional approaches have not yet enabled the data to be converted to ice thickness.

One particularly valuable use of sea ice thickness data would be to quantify the volume flux of ice through important Arctic waterways. Aside from thermodynamic contributions (summer melt and winter growth rates), dynamic fluxes of sea ice through the Fram, Nares and Bering Straits regulate total ice mass balance for the Arctic Ocean. Past studies have calculated the area flux of sea ice through these gateways by integrating remotely sensed observations of ice concentration and drift (Kwok, et al., 2004; Howell, et al., 2013), discovering significant interannual variations in ice exchange driven primarily by decadal oscillations in climate, such as the NAO index. However, ice area fluxes do not offer the complete picture – because a year with high area export, but of thin first-year sea ice, may not directly lead to a fall in annual Arctic ice mass balance. Estimates for the winter Fram Strait ice volume flux have been made using airborne electromagnetic (AEM) induction surveys of ice thickness (Krumpen, et al., 2016), but these surveys do not offer anywhere close to the spatiotemporal data coverage of altimetry. Thus, altimeter missions such as Cryosat-2 offer the potential for characterizing long-term interannual sea ice volume export with an unprecedented degree of confidence.

3.2 Methods

The Synthetic Aperture Interferometric Radar Altimeter (SIRAL) of Cryosat-2 operates at Ku-band, with a central frequency of 13.6 GHz (Wingham, et al., 2006). In theory, at incidence angles close to nadir an electromagnetic wave at this frequency should penetrate the snowpack on sea ice and be scattered by the snow-ice interface (Kwok, 2014). However, there is considerable uncertainty in the sensitivity of Ku-band scattering mechanisms to snowpack properties (i.e. temperature, salinity and density) e.g. (Nandan, et al., 2017), so that it is not clear where the mean scattering surface is located within snow-covered sea ice. A significant advantage of sensing sea ice in summer with SIRAL is that, without snow, we can expect the mean scattering surface to always be located at the sea ice surface. The penetration depth of Ku-band into warm (>-5 °C) first-year sea ice is less than 2 cm and sub-millimeter into fresh melt pond water (Hallikainen & Winebrenner, 1992). This provides the physical basis for Ku-band altimeter measurements of sea ice freeboard in summer – we expect the radar echoes to scatter from the surfaces of sea ice, melt ponds and/or ocean water. So, ice freeboard can theoretically be detected, as long as echoes from the ice and ocean surfaces can be distinguished.

In winter, sea ice and lead returns can be effectively separated through variations in the geometrical properties of waveforms, such as the stack standard deviation and pulse peakiness, as described above. The theoretical model for an altimeter echo is expressed as a double-convolution of the radar transmit pulse, surface height probability density function (PDF), and the 'rough surface' impulse response (Wingham, et al., 2018). Therefore, multilooked SAR echoes from rougher surfaces are wider (less 'peaky') because the backscattered signal is a product of scattering from a range of elevations and incidence angles, covering a larger portion of the effective altimeter footprint (Galin, et al., 2013). The echo from a flat dielectric surface is sharply peaked because most of the backscattered signal comes from a small area around nadir, at the very center of the footprint. Sea ice is relatively rough in comparison to a lead, so appears like the former (Kurtz, et al., 2014). However, during summer, meltwater at the sea ice surface modifies the impulse response of the ice, enhancing the backscattered signal from nadir and producing a quasi-specular return comparable to a lead. A series of these peaked echoes from melt pond-covered sea ice are illustrated in blue in Figure 1a.

Our approach in Arctic-SummIT was to investigate the possibility of a machine learning algorithm, or set of algorithms, performing the classification to separate radar echoes from melt pond covered sea ice and leads. Echoes from leads evidently have different backscattering properties to those from melting sea ice (Figure 1a); however, the specific characteristics of these waveform shape differences was found to vary between regions, ice concentrations and different parts of the summer melting season. Provided with the correct, representative training data, a machine learning approach could learn these variable waveform parameter differences. The first major task of the project was to identify high-resolution imagery from independent satellites, coinciding with CryoSat-2 orbits, from which we could obtain sea ice and lead samples for training and testing the classifier. A set of 550 RADARSAT-2 SAR images were provided by project partners from Environment Canada. Additional SAR imagery was obtained from Sentinel-1A&B and optical imagery from Sentinel-2 and Landsat-8. Following the launch of Sentinel-1B, we identified around 100 images per month with some spatial overlap with CryoSat-2 orbits and coinciding within 15 minutes to account for ice drift (below). Usually only around 20 of these provided a full image overlap.

Sensor	**Coincident Images per Month**
Sentinel-1A/B	~90
Sentinel-2	~5
Landsat-8	~7
RADARSAT-2	~7

CryoSat-2 observations were acquired from the ESA GPOD SARvatore altimetric toolbox service. Most of the observations used were from 2011-2019 pan-Arctic SAR and SARIn processing jobs, now stored on the SARvatore data repository (see Data section). These datasets contained CryoSat-2 waveforms processed to Level 1B, including the surface elevation estimated from a semi-analytical echo model fit to radar waveforms and the range integrated power (RIP), both unavailable in the ESA official CryoSat-2 L1B product. The SARvatore processor fits the SAMOSA+ waveform model to observed echoes (Dinardo, et al., 2018), retracking the timing of the window delay based on the theoretical epoch (mean elevation of the target sea ice surface). SAMOSA+ has been shown to produce good estimates for the range to and thus surface elevation of sea ice targets, as well as coastal waters and inland waters (Dinardo, et al., 2018). The RIP is the delay-Doppler radar map summed in the orthogonal direction and acts as an additional waveform parameter for interpreting the echoes. We developed another radar altimeter waveform model over the course of the grant (Landy, et al., 2019), the so-called facet-based echo model (Matlab code available https://github.com/jclandy/FBEM), which has been applied to winter CryoSat-2 waveform observations over the Arctic (Landy, et al., 2020). Examples for the fits of FBEM model solutions to L1B CryoSat-2 echoes are shown in Figure X, in a similar process to SARvatore. However, after testing the application of FBEM to CryoSat-2 data in summer we decided – both for ease of use and time – to use the dataset already available on the GPOD repository. We additionally ran 15-20 of our custom jobs on SARvatore at the higher 80 Hz posting rate, compared to the normal 20 Hz posting, to assess whether the higher ~80 m along-track resolution might better discriminate thin leads in the ice pack.

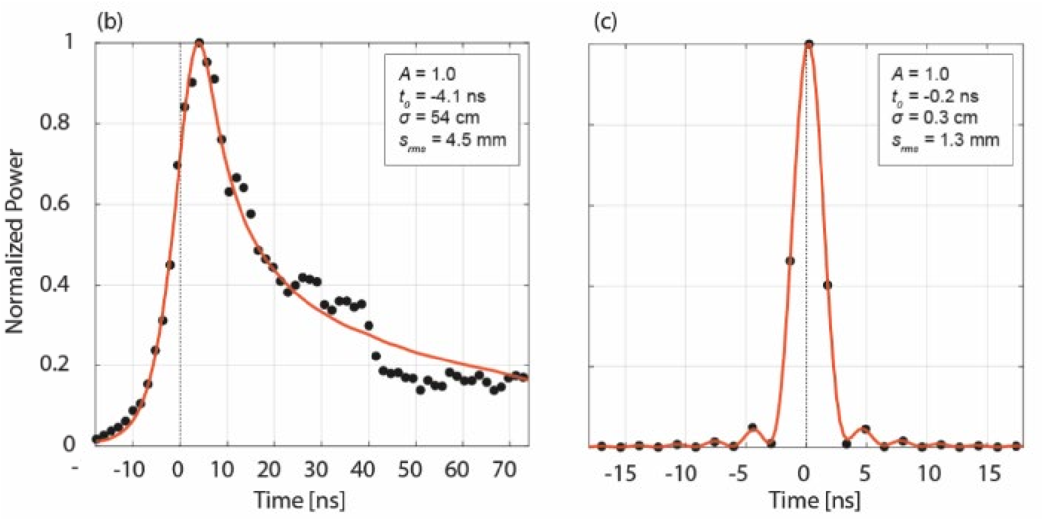

Figure 2. | a. Theoretical radar altimeter echo modelled from FBEM fit to a L1B CryoSat-2 SAR waveform backscattered from winter sea ice. **b.** theoretical echo fit to a lead waveform. Inset values are the waveform amplitude, epoch, surface roughness, and mean square slope optimized from the theoretical model fit to the waveform (Landy, et al., 2020).

CryoSat-2 samples along the satellite orbit were aligned to coinciding SAR or optical satellite imagery with a custom-built Matlab GUI (designed by G. Dawson). This GUI shows the radar waveform and RIP for a chosen sample along track, and the local Ku-band backscattering coefficient σ^0 and elevation (from SAMOSA+ retracking) for a 5 km window around the sample (Fig. 3). More than 100 lead samples were identified where the waveform parameters for a given sample showed strong deviations from their neighbors and a lead could be confirmed in the satellite image. Figure 3 illustrates a valid lead sample manually identified from the training imagery. Sea ice samples were identified where there was no evidence for a lead or other speckle feature in the coinciding imagery. We manually selected >100 lead samples and >200 sea ice samples in this manner. Following early experiments, we discovered that the CryoSat-2 elevation and σ^0 observations over melting sea ice exhibited significant noise (incoherent variability). Noisy samples were particularly evident around valid leads (e.g. Fig. 3), possibly because the radar footprint covers multiple surface types in these regions or more easily 'snags' onto off-nadir specular features like leads. It is important for the machine learning algorithm to include a noise category if significantly different from retrievable classes like sea ice or leads, so we further identified >300 random 'noise' samples from the training imagery.

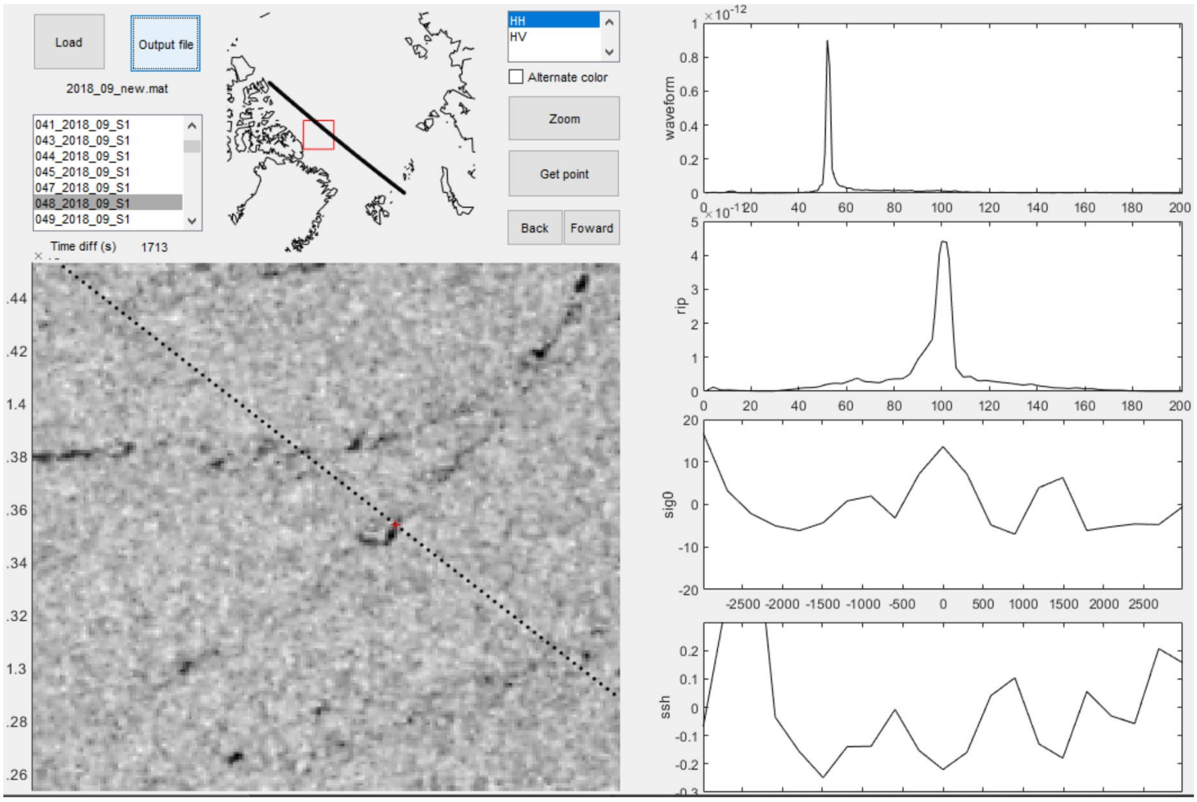

Figure 3 | Simple GUI to generate sea ice, lead and noise training samples for the waveform classification. The Sentinel-1 SAR image footprint and CryoSat-2 orbit are shown in the upper map. Waveform parameters and local observations are shown to the right. The manually selected 'lead' sample is highlighted in red.

General patterns from the manually identified training samples are shown in Figure 4, where local variations in RIP, pulse peakiness, σ^0 and elevation are normalized and centered on the sample. Lead samples exhibit clear oscillations in the 1st derivative for parameters around the lead. Sea ice samples exhibit no obvious change in the 1st derivative but evidently stable local windows in σ^0 and elevation. Noise samples exhibit random distributions in all local parameters. We use the absolute values for all these parameters as the basis for our machine learning classification, but also the distributions in parameters within a hierarchy of window sizes around the sample too.

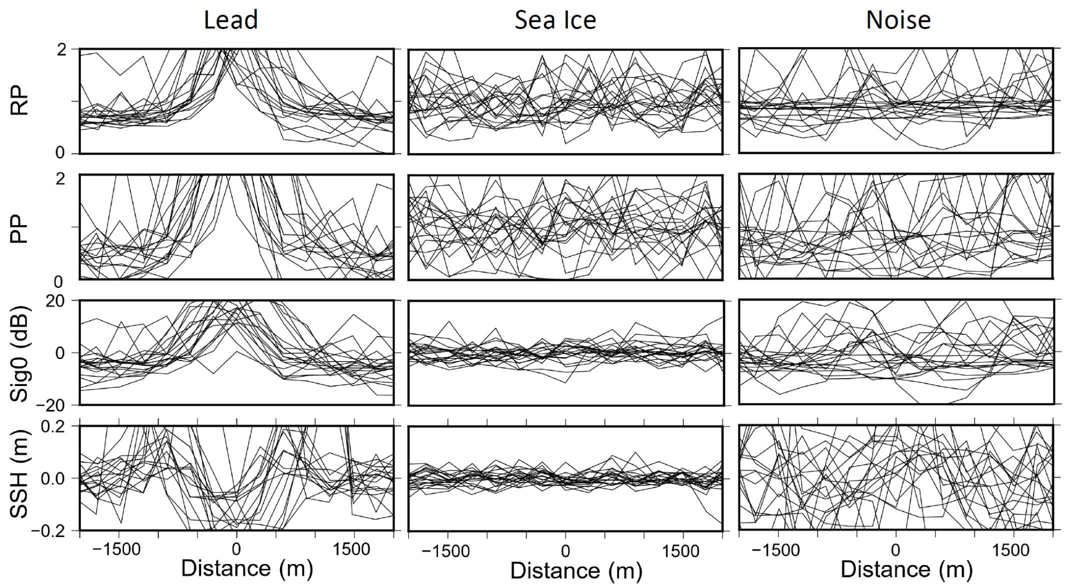

Figure 4 | Local variations in select waveform parameters within 4 km windows around the manually identified training samples. RP = range integrated power, PP = pulse peakiness, Sig0 = backscattering coefficient, SSH = elevation from SAMOSA+ retracking.

We have tested many different options for classifying the CryoSat-2 samples into sea ice , lead and noise classes; however, we report on two chosen strategies: one shallow and one deep learning algorithm. For the shallow learning algorithm we used SciKit, a common Python based classification toolbox https://scikit-learn.org/stable/. We employed a decision tree algorithm because it is simple, easy to track the algorithm decisions about specific parameters, and offers estimates for the final 'importance' of different training features. We used twelve parameters from the short spatial series shown in Figure 4. Parameters for tree building are defined by running model iteratively and testing output stability, with the GINI index providing a measure of the 'purity' of a final class output. An 80-20% split was used to separate between samples for training and testing the model, respectively.

For the deep learning algorithm we used a 1D convolution neural network (CNN), from the KERAS + TensorFlow software https://keras.io/. This algorithm takes in short 1D spatial series of data which, in our case, are the local windows of parameters around training samples (Fig. 5). The CNN uses multiple layers with different feature detectors/filters with different kernel sizes to identify simple or more complex patterns in the input data. Pooling layers extract the main features, containing the majority of the signal, and discard redundant features – thereby preventing overfitting. The 1D CNN produces a PDF of classification uncertainty over the output feature classes. In the schematic example in Figure 5, the CNN identifies >1000 useful parameters from the input spatial data series from which to classify the CryoSat-2 samples. The same 80-20% split was used between training and testing.

The final accuracies of each classification algorithm was 70% for the decision tree and 81% for the 1D CNN, between all three categories: melting sea ice, lead and noise. This represents a significantly better capability for classifying the samples than random chance (i.e., 33%). The accuracies are lower than strict parameter-based machine classifiers for separating winter sea ice samples from leads (Lee, et al., 2016), which produce accuracies of 90+%. However, our summer sea ice classifier is comparable in accuracy to less conservative winter classifiers which provide a more realistic number of leads for the ice concentration but more commission errors (Lee, et al., 2016). We hereafter show results using the 1D CNN classifier applied to the full CryoSat-2 dataset, including zones outside our training areas.

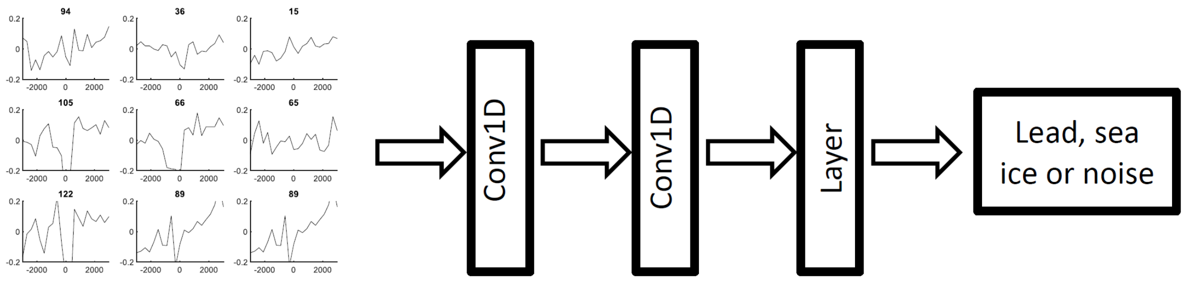


```
=================================================================
Total params: 1,091 Trainable params
```

Figure 5 | Schematic diagram of the typical 1D CNN workflow. TensorFlow takes in the raw CryoSat-2 spatial series themselves as input (rather than derived parameters or subset windows). Multiple layers have different purpose: to identify patterns, pool features and prevent overfitting.

Given that CryoSat-2 samples are classified as ‘noise’ up to 60% of the time over summer sea ice, we could not derive sea ice radar freeboards in the conventional way (i.e., interpolating the sea level between local lead samples along track). We filter out all samples classified as noise and apply further filters to remove clearly erroneous sea ice samples. We then fit a robust polynomial function to all ‘sea ice’ samples within an 8-km window around each ‘lead’ sample. Radar freeboard is then obtained from the difference between fitted sea ice elevation and the lead elevation. This process helps to smooth out the universal along-track variability and speckle apparent in the summer elevation observations. Radar freeboards are interpolated onto both 80 km and 160 km pan-Arctic grids using an inverse-distance weighting algorithm, weighted by sample distance and time to the grid cell. We use the rmse of polynomial sea ice fits and lead classification uncertainties to obtain a preliminary estimate for the overall uncertainty of the grid cell radar freeboard.

CryoSat-2 L1B observations from SARvatore at an 80 Hz posting rate were used to assess possible biases in lead elevations in the 20 Hz observations (see results). SARIn observations at 20 Hz were also used to test the off-nadir distance of the first phase coherent target over melt-pond covered sea ice, applying the approach of (Armitage & Davidson, 2013), so we could evaluate the reliability of elevation estimates. If the radar is continuously snagged to the nearest coherent melt pond target, at different distances from the nadir point for consecutive along track samples, this would introduce a strong (but random) ranging error. However, we found the 1 sigma off-nadir ranging distance was within 100 m for a number of tested orbits over sea ice within the ‘Wingham Box’.

3.3 Data

The following datasets were used in Arctic-SummIT to train & test the classification algorithm, calculate sea ice freeboards, filter valid freeboards and analyze results:

- CryoSat-2 L1B SAR mode 20 Hz waveform observations from the GPOD SARvatore processor, available from the repository ftp://repository:RSS_service@eogrid.esrin.esa.int/0045
- CryoSat-2 L1B SARIn mode 20 Hz waveform observations from the GPOD SARINvatore processor, available from the repository ftp://repository:RSS_service@eogrid.esrin.esa.int/0046
- Custom processed L1B SAR and SARIn mode 80 Hz waveform observations from the GPOD SARvatore altimetric toolkit, 15-20 orbits, here https://gpod.eo.esa.int/
- 500+ Sentinel-1A&B images L2 GRD from https://scihub.copernicus.eu/
- 100+ Sentinel-2 images L2 from https://scihub.copernicus.eu/
- 550 RADARSAT-2 images L2 GRD project partners at Environment Canada (Steve Howell and Alex Komarov). Authorization provided by the data supplier: Macdonald, Dettwiler and Associates (MDA) to use this set of imagery in our project. Not available publicly.
- OSI-401-b: SSMIS Sea Ice Concentration Maps on 10 km Polar Stereographic Grid, freely available at http://osisaf.met.no/p/ice/
- OSI-403-c: Sea Ice Type Maps on 10 km Polar Stereographic Grid, freely available at http://osisaf.met.no/p/ice/
- Beaufort Gyre Exploration Project (BGEP) upward looking sonar observations mooring A, B, and D, available here https://www.whoi.edu/page.do?pid=160656

3.4 Results

Owing to the high noise floor in the summer elevation data and the need to accumulate a lot of data to get good results, with our current approach we're limited to a best resolution of around 80 km. Grids based on one month of freeboard samples at 80 km generally still contain regions of missing data, particularly in May, June and July when the sea ice floes are expected to have highest melt pond coverage and be at their most specular (i.e., similar to leads) (Kwok, et al., 2018). In these missing regions there are insufficient leads classified to obtain valid freeboards.

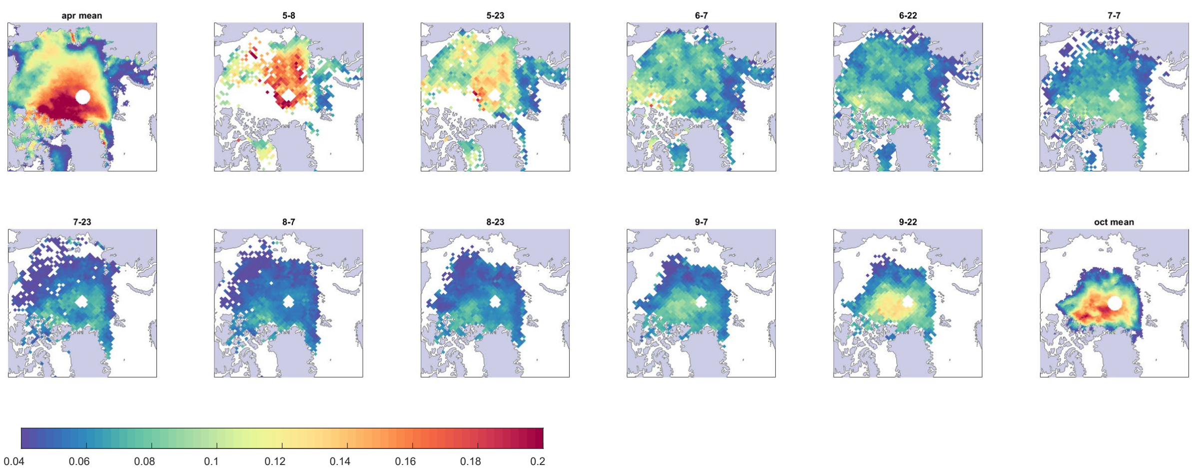

Figure 6 | Climatology of 80-km gridded radar freeboards [m] 2011-2019, including one month of data, at bi-weekly intervals. The April and October mean radar freeboard grids which bookend our new dataset are from the LARM processing chain of (Landy, et al., 2020).

Figure 6 illustrates the climatology of 80-km radar freeboards for all years between 2011 and 2019. We have included mean radar freeboard maps for the months of April and October, i.e. the two cold season maps that bookend our new summer freeboard dataset, derived from the application of the FBEM physical echo model to CryoSat-2 observations (Landy, et al., 2019). The processing chain to obtain this Oct-April dataset for 2010-2019 is described in (Landy, et al., 2020) and the dataset itself is available here: *Arctic sea ice and physical oceanography derived from CryoSat-2 Baseline-C Level 1b waveform observations, Oct-Apr 2010-2018* https://data.bas.ac.uk/full-record.php?id=GB/NERC/BAS/PDC/01257b (Funding acknowledged from ESA Living Planet Fellowship Arctic-SummIT grant ESA/4000125582/18/I-NS and NERC Project PRE-MELT grant NE/T000546/1). The summer radar freeboard patterns in Figure 6 appear quite realistic when compared with the (conventionally processed) April and October thickness fields. The early May and late September fields appear almost identical to the April and October means. There is a clear pattern of ice melting and ice edge retreat throughout June, July and August, before ice thickening begins again in mid-September.

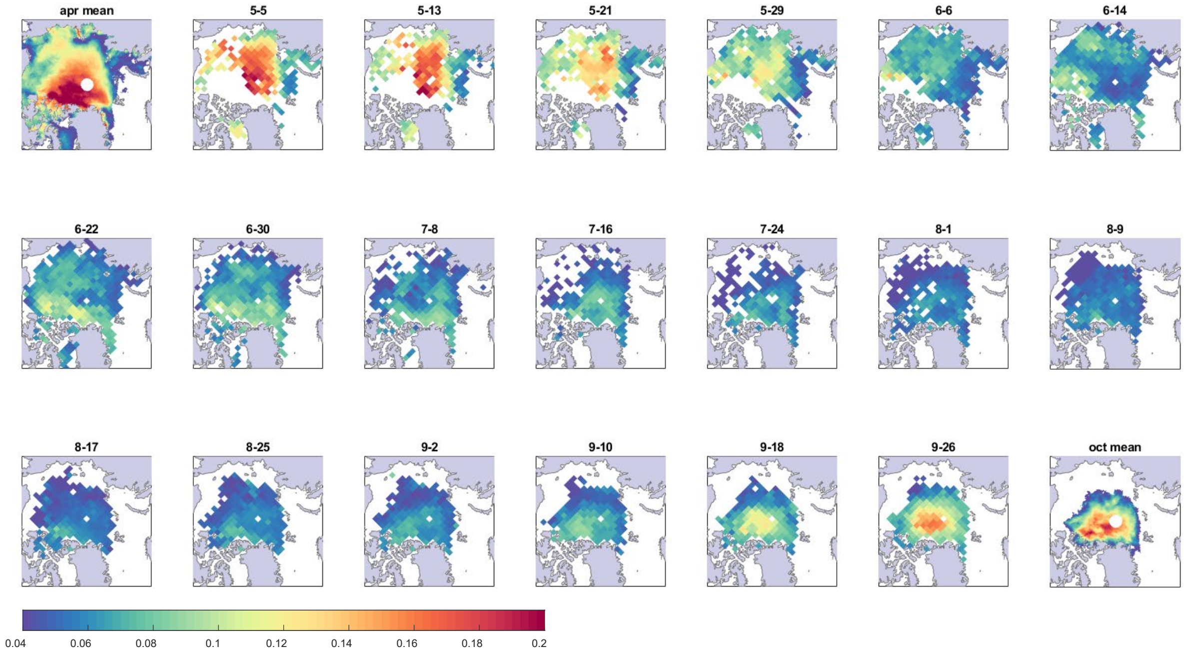

Figure 7 | Climatology of 160-km gridded radar freeboards [m] 2011-2019, including two weeks of data, at weekly intervals. The April and October mean radar freeboard grids which bookend our new dataset are from the LARM processing chain of (Landy, et al., 2020).

Because the majority of sea ice in summer is clustered around the pole, where the CryoSat-2 orbits converge, we can reduce the spatial resolution of the grid to 160 km and obtain approximately weekly freeboard fields (Fig. 7). These highlight changing snowpack properties from April into May, with an apparently rapid increase in freeboards in the Beaufort Sea and Eastern Arctic by the end of May. As the snow gets warmer and wetter following melt onset in the Arctic, the Ku-band CryoSat-2 radar will be prevented from penetrating into the snow. So, the May radar freeboards appear to show approximately total snow plus sea ice freeboards, rather than sea ice thickening (which is unrealistic). The freeboards start to decline in late-May/early

June, before thinning significantly between June and mid-August. There is sea ice thinning and then total loss and ice edge retreat through August, for example in the Beaufort and Chukchi Seas (Fig. 7). Some ice thickening is clear over the remaining Central Arctic ice pack during September.

To assess the validity of these new freeboard observations, we converted freeboards to estimates for the sea ice draft by applying a simple constant density conversion for all summer grids. Woods Hole Oceanographic Institute have deployed underwater moorings in the Beaufort Sea for many years, with upward looking sonars that can measure the ice draft (the portion of the ice floating below sea level). So, we compared ice drafts estimated from our CryoSat-2 data to the time-series of drafts measured at the mooring locations. In Figure 8, we show the Beaufort Gyre Exploration Program (BGEP) Mooring A, including our satellite data from winter months (black points) (Landy, et al., 2020) and the new data from summer months (red points). The data match quite closely, capturing most of the full sea ice freeze-up and melting seasons. It is encouraging that the crossover time periods between datasets from the 'cold' and 'warm' periods match up well. For instance, the high summer ice year of 2013 and low years of 2012 and 2016. However, there does appear to be some underestimation of total draft at the start of summer (May) reflecting the fact we haven't corrected for a snow load in any of the summer months, including May.

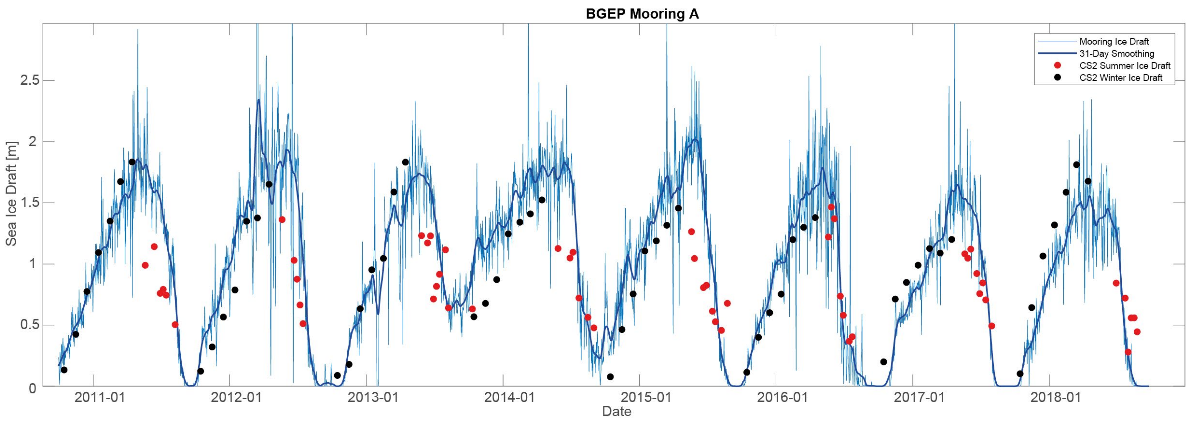

Figure 8 | Sea ice draft measured at the upward looking sonar on BGEP Mooring A (blue line), with a 31-day moving average applied (solid blue line). Coinciding satellite ice drafts measured by CryoSat-2 in winter months Oct-Apr (black points) and summer months May-Sept (red points).

The comparison to airborne sea ice thickness data from the AWI "IceBird" Program (courtesy of Dr. Thomas Krumpen), for Arctic-SummIT Objective C, is not as encouraging. We have compared four years of IceBird sea ice campaigns in August-September, 2011, 2016, 2017 and 2018, to the CryoSat-2 freeboard estimates. An ice density of 916 kg/m3 was used to convert radar freeboards to ice thickness. We have found that CryoSat-2 ice thickness underestimates the airborne electromagnetic induction (AEM) sensor in all flight campaigns (Fig. 9). Over the marginal sea ice sampled in 2011, CryoSat-2 underestimates the AEM by 40-50 cm. Over the Central Arctic pack ice (the thickest sea ice in the Arctic) in 2016-2018, it underestimates the ice thickness by around 100 cm. A significant part of our research that was not anticipated at the proposal stage has therefore involved examining why this is the case.

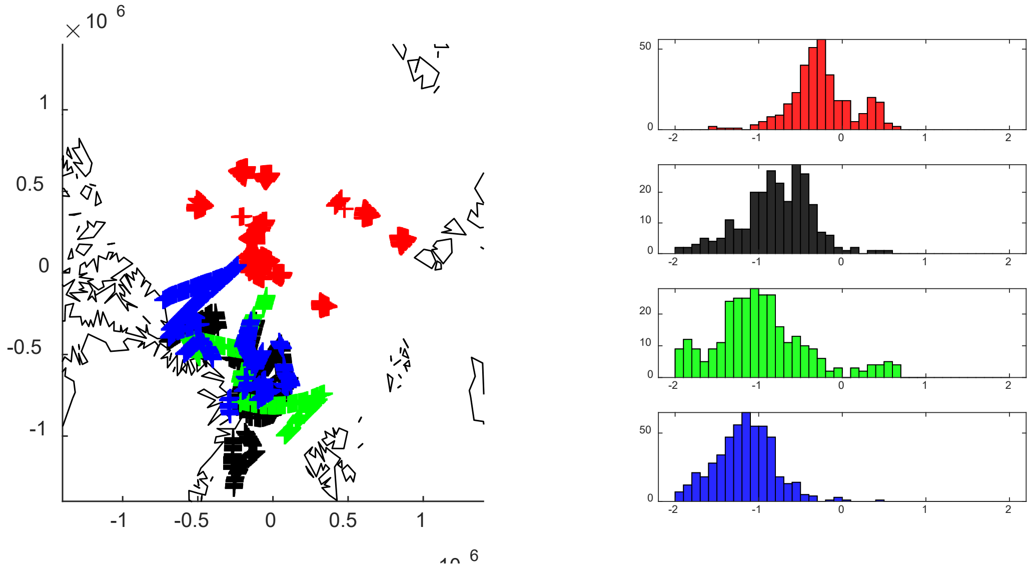

Figure 9 | a. Sea ice campaigns flown by the AWI "IceBird" Program, in 2011 (red), 2016 (black), 2017 (green), and 2018 (blue). **B.** Histograms of the difference between CryoSat-2 estimated sea ice thickness and AEM thickness [m] (CS2 minus AEM).

We have identified five possible sources for this ice thickness bias. One source may dominate, or multiple sources could be acting together.

1. The range to the sea surface is underestimated at leads, with the radar sensitive to specular scatterers covering just 1% of the sensor footprint (Kwok, et al., 2018). If a CryoSat-2 return classified as a lead comprises reflections from melt ponds closer to the nadir point than a lead, or mixed classes within the pulse-limited footprint (~320 x 1500 m), the retrieved lead elevation could be biased high. This is supported by analysis of sea surface height (SSH) observations from leads between 80 and 20 Hz posted data (i.e., 80 vs 320 m along-track resolution) for the same tracks. The SSH at 20 Hz is above the SSH at 80 Hz, with a median difference of 5 mm (Fig. 10). So, the range from the altimeter to the sea surface is slightly underestimated at the coarser resolution. This would constitute an order 5 cm bias in thickness.

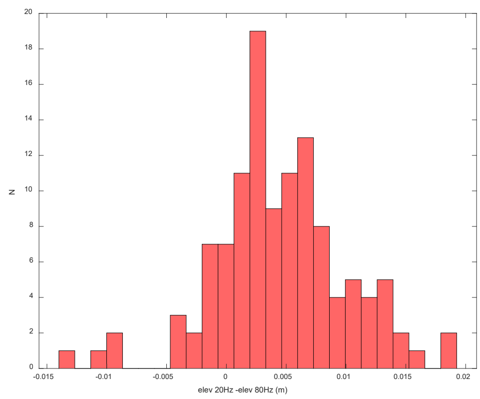

Figure 10 | Sea surface height retracked by SAMOSA+ at leads for 20 Hz versus 80 Hz posted along-track observations. The median difference is 5 mm, so leads are not as well resolved at the coarser 20 Hz footprint, suggesting interference from ice floes/ponds within the footprint.

2. There are some evident differences between the SSH measurements from the GPOD L0 > L1B processor and the official ESA L1B product for CryoSat-2. We have applied a peak retracker to waveforms reliably classified as leads in winter months, for identical tracks from the GPOD L1B archive and ESA L1B archive (with the GPOD tracks processed with an identical chain to the official product). The ESA SSH estimates are on average 7 mm lower than the GPOD SSH estimates, simply from the different L0 > L1B processing chains. This would constitute an order 7 cm underestimation in ice thickness.

3. The effective density of sea ice floes in Arctic summer months could be much higher than 860-910 kg/m3, i.e. the range of densities used for multi-year to first-year sea ice types in winter months (Alexandrov, et al., 2010). If sea ice floes in summer are completely permeable, then air pockets will be filled with ocean water. Thus, the actual density of the liquid filled sea ice below sea level might be much higher than expected. Using an ice density of >930 kg/m3 produces satellite -derived ice thickness estimates more comparable to the airborne observations.

4. If there is a residual snow load on the sea ice or melt pond water accumulated on the ice above sea level, we would need to account for this in the hydrostatic conversion from ice freeboard up to thickness. The following equation has been derived for converting freeboard to thickness in the presence of surface meltwater load above sea level:

$$h_{si} = \left(\frac{\rho_{sw}}{\rho_{sw} - \rho_{si}}\right)\left(h_f + \varepsilon\right) - \left(\frac{\rho_{sw} - \rho_{pw}}{\rho_{sw} - \rho_{si}}\right) f_p h_p$$

Where ρ_{sw} and ρ_{si} are the densities of seawater and sea ice, respectively, f_p is the surface melt pond fraction, ρ_{pw} is the density of pond water and h_p is the pond depth. We can safely assume that ρ_{sw} = 1024 kg m^{-3} e.g. (Ricker, et al., 2014) and ρ_{pw} = 1000 kg m^{-3}. This equation demonstrates that the sensitivity of estimated ice thickness to exaggerated variations in pond fraction (0-100%) and depth (0-50 cm), calculated from Equation 2, is relatively low. For instance, we can expect uncertainty <10% when ice freeboard is greater than 0.1 m.

5. Possibly the most influential bias might be that melt ponds affect the principal scattering horizon of the CryoSat-2 Ku-band radar. For a diffusely scattering sea ice surface in winter months, the radar waveform integrates a backscattered return from sea ice across the pulse-limited footprint – sampling the full height distribution of the ice over this footprint. The theoretical radar retracking point, for instance obtained by fitting SAMOSA+ to waveforms, should accurately identify the mean level of the sea ice surface. This is crucial for estimating the ice freeboard, because any systematic deviation of the principal scattering horizon away from the mean ice level would introduce a bias. (This idea is well documented in ocean altimetry as the so-called electromagnetic (EM) bias). Ponds on the sea ice surface in summer months will produce coherent reflections that dominate the radar waveform, which is why the majority of sea ice echoes are specular (have high pulse peakiness) (Kwok, et al., 2018). The waveform peak is referenced to the surface of reflecting ponds, so if these pond surfaces lie below the mean ice level a positive bias will be added to the range measurement over sea ice.

We have completed a set of numerical experiments with the FBEM waveform model (Landy, et al., 2019) to quantify this final bias, before potentially accounting for it in the conversion from ice freeboard to thickness. We have added random distributions of melt ponds, with a range of coverage, to sea ice surfaces with a range of surface roughness (Fig. 11). Dielectric properties for the melting sea ice and ponds have been obtained from the literature (Scharien, et al., 2014). Our simulations demonstrate that increasing the melt pond coverage at the ice surface produces increasingly specular peaky echoes (Fig. 11a) because the ponds start to dominate the radar return. If the sea ice surface is rougher, the mean pond surface height will lie at an increasingly low level with respect to the mean ice level – leading to a higher freeboard bias (Fig. 11b). We can therefore expect rougher multi-year sea ice in the Central Arctic, with lower surface pond coverage than smoother first-year ice in the marginal Arctic (Landy, et al., 2015), to produce a higher freeboard bias of up to 15 cm (Fig. 11b). The likely range of the freeboard bias would constitute an underestimation in CryoSat-2 summer sea ice thickness of 20-150 cm.

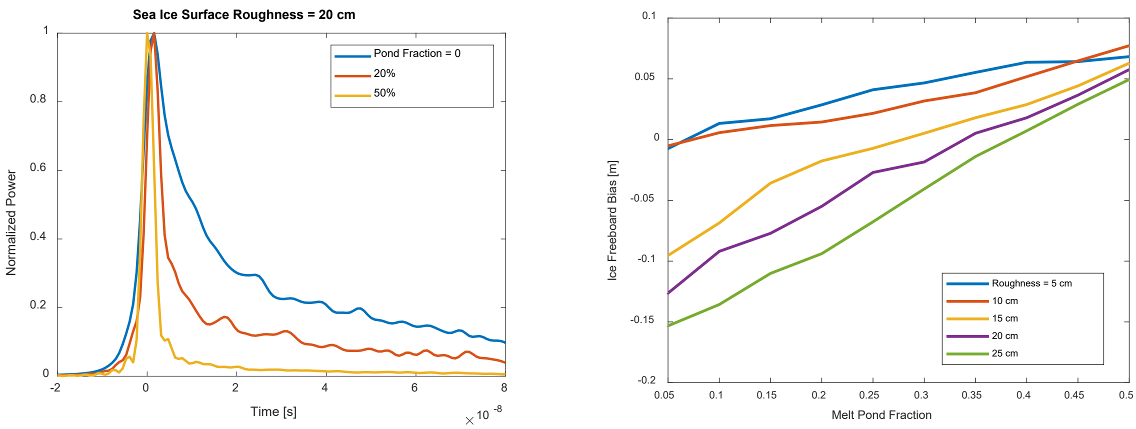

Figure 11 | a. Numerical simulations of the backscattered radar echo from melting sea ice, with a roughness standard deviation of 20 cm, and surface melt pond coverage of 0, 20 and 50%. **B.** The estimated sea ice freeboard bias caused by melt pond surfaces sitting at a different height to the mean ice surface level, within the radar footprint

In our ongoing work, we are attempting to use sea ice roughness observations (Landy, et al., 2020), coinciding measurements of the sea ice melt pond fraction (https://seaice.uni-bremen.de/melt-ponds/) and these simulation results to produce pan-Arctic corrections for the measured CryoSat-2 radar freeboard. These corrections will be applied to the freeboards before converting to ice thickness and re-validated against the available AEM thickness data from AWI (Fig. 9). Once these corrections have been developed, we will disseminate Version 1 of the CryoSat-2 sea ice thickness product including uncertainties, to the BAS Polar Data Centre.

We have not yet been able to confront Objective D of Arctic-SummIT, requiring the sea ice thickness product to be finalized before integrating with ice drift to obtain volume fluxes. Our partners at EC have produced a weekly sea ice motion product from RADARSAT-2 and Sentinel-1A&B, available since 2016 (Howell, et al., 2018), which we will use to study sea ice volume fluxes across Nares Strait, Fram Strait, and Bering Strait. We will use the combined winter and summer sea ice thickness data (Fig. 8) to estimate several full years of volume fluxes across the key Arctic gateways.

4 CONCLUSIONS AND RECOMMENDATIONS

Arctic-SummIT has confirmed that to obtain valid Arctic sea ice thickness data in summer from CryoSat-2 is a huge challenge! However, in spite of the challenges, we have made several major steps here towards achieving this goal. We have developed several machine learning classification algorithms, with shallow and deep learning strategies, for separating CryoSat-2 echoes from leads and melt pond-covered sea ice. The algorithms have been trained on and tested against a set of hundreds of coincident satellite images from Sentinel-1A&B, RADARSAT-2, Sentinel-2, and Landsat-8. We obtain classification accuracies up to 81% for the deep learning algorithm versus independent testing samples, which are not far short of the accuracies of classical waveform-parameter based threshold classifiers applied to cold season altimeter observations.

Sea ice radar freeboards derived from the CryoSat-2 sea ice and lead echoes reflect expected spatial and temporal patterns in summer melt evolution. Gridded radar freeboard fields are produced at 80-km resolution on biweekly timescales and 160-km resolution on weekly timescales. The Ku-band radar scattering horizon becomes elevated as the snowpack begins to melt in May, producing thicker than expected radar freeboards. Sea ice thins between June and August, with clear thinning before ice edge retreat in the marginal Arctic seas. Sea ice begins to thicken in the Central Arctic from mid-September. Comparisons with sea ice draft observations from the in situ ULS at BGEP moorings demonstrate that CryoSat-2 can capture the full annual ice evolution in the Beaufort Sea. However, CryoSat-2 estimates for sea ice thickness typically underestimate coincident airborne EM observations.

We have identified multiple possible causes for this thickness bias and have completed numerical waveform modelling experiments to characterize the most dominant source of bias. In our future work, we will develop a generalized bias correction for freeboard-to-thickness conversion from CryoSat-2 sea ice surface roughness observations and MERIS melt pond fraction data. We will finish validating the satellite ice thickness product against ULS and airborne EM observations, constraining the data product uncertainties. Finally, we will obtain sea ice volume fluxes at key Arctic gateways across the entire annual season, for the first time, by integrating the new sea ice thickness data with SAR ice motion observations. The importance of summer Arctic sea ice thickness data to the research community has been confirmed with our success gaining grant funding from NERC to build on the progress of Arctic-SummIT. The PRE-MELT project will support our continued developmental work, but we will acknowledge ESA funding in all relevant future manuscript submissions.

Scientific roadmap for follow-on work

We make the following recommendations for future work in this field, which could be supported by future ESA research funding:

1. Our preliminary research with higher posted 80 Hz CryoSat-2 observations suggests there may be some advantage of using these finer sampled data over sea ice in summer months. We recommend that further tests are made with 80 Hz observations, potentially intercomparing results for a full summer season between 80 and 20 Hz processed sea ice freeboards.

2. To test our classification and ice freeboard retrieval algorithms on Sentinel-3A&B. We anticipate that the existing algorithms could be applied to Setinel-3 SRAL altimeters exactly as they have been for CryoSat-2. This would enable sub-weekly sampling of sea ice freeboard in summer months, would significantly reduce the regions of missing data in current CryoSat-2-only freeboard fields, and produce more valid lead returns to improve the reliability of derived freeboard grids. It might be necessary to wait for the new version of Sentinel-3 SRAL processing over sea ice regions, so that Sentinel-3 L1B observations perfectly match those of CryoSat-2.

3. Pan-Arctic summer melt pond fraction data will be crucial for converting the derived radar freeboard fields to thickness. Pond fraction is important for both the freeboard bias introduced by specular radar reflections from pond surfaces and for estimating the volume of pond water loading the ice above sea level, to accurately solve the hydrostatic equation. We would recommend future support for projects building melt pond fraction datasets from optical satellite sensors.

4. Early research suggests that it might be possible to measure sea ice freeboard and thickness with NASA's ICESat-2, following continued developmental work (Tilling et al., 2020). With CryoSat-2 now operating alongside ICESat-2, with a migrated orbit producing 20+ profiles of coinciding along-track observations every month, in the *Cryo2Ice* campaign. Future research should focus on intercomparing CryoSat-2 freeboards and ICESat-2 sea ice properties along coincident profiles – provided CryoSat-2 continues to operate as normal, this multi-mission study will be possible following summer 2021.

5. The reference AEM sea ice thickness observations from our AWI partners have been and will continue to be crucial for validating derived ice thickness products from CryoSat-2 (or Sentinel-3, ICESat-2) in summer months. We would recommend that ESA consider future CryoVex airborne sampling campaigns over sea ice during summer months (May-Sept) – including the thickest multi-year ice in the Central Arctic, but also the thinner decaying ice in the marginal seas. Airborne radar altimeter and aerial photograph observations over pond-covered sea ice would support improved classification algorithm development and training, complimenting the EM ice thickness measurements.

5 REFERENCES

Alexandrov, V., Sandven, S., Wahlin, J. & Johannessen, O., 2010. The relation between sea ice thickness and freeboard in the Arctic. *Cryosphere,* 4(3), pp. 373-380.

Allard, R. et al., 2018. Utilizing CryoSat-2 Sea Ice Thickness to Initialize a Coupled Ice-Ocean Modeling System. *Adv. Space Res.,* Volume In Press.

Armitage, T. & Davidson, M., 2013. Using the Interferometric Capabilities of the ESA Cryosat-2 Mission to Improve the Accuracy of Sea Ice Freeboard Retrievals. *IEEE Trans. Geosci. Rem. Sens.,* 52(1), pp. 529-536.

Arrigo, K. R., Perovich, D. K., Pickart, R. & Zachary, W. B., 2012. Massive Phytoplankton Blooms Under Arctic Sea Ice. *Science,* Volume 336, p. 1408.

Barber, D. et al., 2015. Selected physical, biological and biogeochemical implications of a rapidly changing Arctic Marginal Ice Zone. *Prog. Oceanog.,* Volume 139, pp. 122-150.

Barnhart, K., Miller, C., Overeem, I. & Kay, J., 2016. Mapping the future expansion of Arctic open water. *Nature Clim. Chan.,* 6(3), p. 280.

Chen, Z. et al., 2017. Impacts of Assimilating Satellite Sea Ice Concentration and Thickness on Arctic Sea Ice Prediction in the NCEP Climate Forecast System. *J. Clim.,* 30(21), pp. 8429-8446.

Day, J., Hawkins, E. & Tietsche, S., 2014. Will Arctic sea ice thickness initialization improve seasonal forecast skill?. *Geophys. Res. Lett.,* 41(21), pp. 7566-7575.

Dinardo, S. et al., 2018. Coastal SAR and PLRM altimetry in german bight and west baltic sea. *Adv. Space Sci.,* 62(6), pp. 1371-1404.

Galin, N. et al., 2013. Calibration of the CryoSat-2 interferometer and measurement of across-track ocean slope. *IEEE Trans. Geosci. Rem. Sens.,* 51(1), pp. 57-72.

Guemas, V. et al., 2016. A review on Arctic sea-ice predictability and prediction on seasonal to decadal time-scales. *Quat. J. Royal Met. Soc.,* 142(695), pp. 546-561.

Hallikainen, M. & Winebrenner, D., 1992. The Physical Basis for Sea Ice Remote Sensing. In: F. Carsey, ed. *Microwave Remote Sensing of Sea Ice*. Washington DC: American Geophysical Union Monograph Series, pp. 30-46.

Howell, S. et al., 2018. Comparing L-and C-band synthetic aperture radar estimates of sea ice motion over different ice regimes. *Rem. Sens. Env.,* Volume 204, pp. 380-391.

Howell, S. et al., 2013. Recent changes in the exchange of sea ice between the Arctic Ocean and the Canadian Arctic Archipelago. *J. Geophys. Res. Oceans,* 118(7), pp. 3595-3607.

Kaleschke, L. et al., 2012. Sea ice thickness retrieval from SMOS brightness temperatures during the Arctic freeze-up period. *Geophys. Res. Lett.,* Volume 39, p. L05501.

Krumpen, T. et al., 2016. Recent summer sea ice thickness surveys in the Fram Strait and associated volume fluxes. *Crysophere,* 10(2), p. 523.

Kurtz, N., Galin, N. & Studinger, M., 2014. An improved CryoSat-2 sea ice freeboard retrieval algorithm through the use of waveform fitting. *Cryosphere,* Volume 8, pp. 1217-1237.

Kwok, R., 2014. Simulated effects of a snow layer on retrieval of CryoSat-2 sea ice freeboard. *Geophys. Res. Lett.,* Volume 41, pp. 5014-5020.

Kwok, R. & Cunningham, G., 2015. Variability of Arctic sea ice thickness and volume from Cryosat-2. *Phil. Trans. R. Soc. A,* 373(20140157).

Kwok, R., Cunningham, G. & Armitage, T., 2018. Relationship between specular returns in CryoSat-2 data, surface albedo, and Arctic summer minimum ice extent. *Elem. Sci. Anth.,* 6(1), p. 53.

Kwok, R., Cunningham, G. & Pang, S., 2004. Fram Strait sea ice outflow. *J. Geophys. Res. Oceans,* 109(C1).

Kwok, R., Cunningham, G., Zwally, H. & Yi, D., 2007. Ice, Cloud, and land Elevation Satellite (ICESat) over Arctic sea ice: Retrieval of freeboard. *J. Geophys. Res.,* Volume 112, p. C12013.

Kwok, R., Spreen, G. & Pang, S., 2013. Arctic sea ice circulation and drift speed: Decadal trends and ocean currents. *J. Geophys. Res. Oceans,* 118(5), pp. 2408-2425.

Landy, J. et al., 2017. Sea ice thickness in the Eastern Canadian Arctic: Hudson Bay Complex & Baffin Bay. *Rem. Sens. Env.*.

Landy, J., Ehn, J. & Barber, D., 2015. Albedo feedback enhanced by smoother Arctic sea ice. *Geophys. Res. Lett.,* 42(24), pp. 10714-10720.

Landy, J., Petty, A., Tsamados, M. & Stroeve, J., 2020. Sea ice roughness overlooked as a key source of uncertainty in CryoSat-2 ice freeboard retrievals. *J. Geophys. Res. Oceans,* Volume In Press.

Landy, J., Tsamados, M. & Scharien, R., 2019. A Facet-Based Numerical Model for Simulating SAR Altimeter Echoes from Heterogeneous Sea Ice Surfaces. *IEEE Trans. Geosci. Rem. Sens.,* 57(7), pp. 4164-4180.

Laxon, S. et al., 2013. CryoSat-2 estimates of Arctic sea ice thickness and volume. *Geophys. Res. Lett.,* Volume 40, pp. 732-737.

Lee, S. et al., 2016. Arctic sea ice thickness estimation from CryoSat-2 satellite data using machine learning-based lead detection. *Rem. Sens.,* 8(9), p. 698.

Morison, J. et al., 2012. Changing Arctic Ocean freshwater pathways. *Nature,* Volume 481, pp. 66-70.

Nandan, V. et al., 2017. Effect of Snow Salinity on CryoSat-2 Arctic First-Year Sea Ice Freeboard Measurements. *Geophys. Res. Lett.,* 44(20), p. 10419–10426.

NSIDC, 2018. *Arctic Sea Ice News.* [Online]
Available at: http://nsidc.org/arcticseaicenews/
[Accessed January 2018].

Overland, J. et al., 2015. The melting Arctic and midlatitude weather patterns: Are they connected?. *J. Clim.,* 28(20), pp. 7917-7932.

Ricker, R. et al., 2014. Sensitivity of CryoSat-2 Arctic sea-ice freeboard and thickness on radar-waveform interpretation. *Cryosphere,* Volume 8, pp. 1607-1622.

Scharien, R., Landy, J. & Barber, D. G., 2014. First-year sea ice melt pond fraction estimation from dual-polarisation C-band SAR–Part 1: In situ observations. *The Cryosphere,* 8(6), pp. 2147-2162.

Schroeder, D. et al., 2017. *Using CryoSat-2 sea ice thickness distribution to constrain the CICE sea ice model.* Vienna, Austria, EGU General Assembly Conference Abstracts, p. 17066.

Schweiger, A. et al., 2011. Uncertainty in modeled Arctic sea ice volume. *J. Geophys. Res.,* Volume 116, p. C00D06.

Serreze, M. et al., 2009. The emergence of surface-based Arctic amplification. *Cryosphere,* Volume 3, pp. 11-19.

Stroeve, J. et al., 2012. The Arctic's rapidly shrinking sea ice cover: a research synthesis. *Climatic Change,* 110(3-4), pp. 1005-1027.

Tian-Kunze, X. et al., 2014. SMOS-derived thin sea ice thickness: algorithm baseline, product specifications and initial verification. *Cryosphere,* Volume 8, pp. 997-1018.

Tietsche, S. et al., 2018. Thin sea ice in the Arctic: comparing L-band radiometry retrievals. *Cryosphere Discussions,* p. In Review.

Tilling, R. L., Ridout, A. & Shepherd, A., 2016. Near-real-time Arctic sea ice thickness and volume from CryoSat-2. *Cryosphere,* Volume 10, pp. 2003-2012.

Webster, M. et al., 2014. Interdecadal changes in snow depth on Arctic sea ice. *J. Geophys. Res. Oceans,* Volume 119, pp. 5395-5406.

Wingham, D. et al., 2006. CryoSat: A mission to determine the fluctuations in Earth's land and marine ice fields. *Adv. Space Res.,* 37(4), pp. 841-871.

Wingham, D. et al., 2018. A Semianalytical Model of the Synthetic Aperture, Interferometric Radar Altimeter Mean Echo, and Echo Cross-Product and Its Statistical Fluctuations. *IEEE Trans. Geosci. Rem. Sens.,* Volume In Press.

Zhang, J. & Rothrock, D., 2003. Modeling Global Sea Ice with a Thickness and Enthalpy Distribution Model in Generalized Curvilinear Coordinates. *Mon. Wea. Rev.,* Volume 131, p. 845–861.

Zhang, J. et al., 2008. Ensemble 1-Year predictions of Arctic sea ice for the spring and summer of 2008. *Geophys. Res. Lett.,* 35(8).

6 PUBLICATIONS

Peer-reviewed publications completed during and relating to Arctic-SummIT work:

Landy, J.C., Petty, A., Tsamados, M., Stroeve, J. (2020) Sea ice roughness overlooked as a key source of uncertainty in Cryosat-2 ice freeboard retrievals, J. Geophys. Res. Oceans, 125(5), doi:10.1029/2019JC015820.

Mallett, R.D., Lawrence, I.R., Stroeve, J.C., Landy, J.C. and Tsamados, M., (2020). Brief communication: Conventional assumptions involving the speed of radar waves in snow introduce systematic underestimates to sea ice thickness and seasonal growth rate estimates. Cryosphere, 14(1), 251-260, doi: 10.5194/tc-14-251-2020.

Landy, J.C., Tsamados, M., Scharien, R.K. (2019). A Facet-Based Numerical Model for Simulating SAR Altimeter Echoes from Heterogeneous Sea Ice Surfaces. IEEE Trans. Geosci. Rem. Sens., 57(7), 4164-4180, doi: 10.1109/TGRS.2018.2889763.

Babb, D.G., Landy, J.C., Barber, D., and Galley, R. (2019). Winter sea ice export from the Beaufort Sea as a preconditioning mechanism for enhanced summer melt: A case study of 2016, Journal of Geophysical Research: Oceans. 124(9), 6575-6600, doi: 10.1029/2019JC015053.

Kirillov, S., Babb, D.G., Dmitrenko, I., Landy, J.C., Barber, D.G., Lukovich, J., Ehn, J.K. (2019) Atmospheric forcing drives the winter sea ice thickness asymmetry of Hudson Bay, J. Geophys. Res. Oceans, 125(2), doi: 10.1029/2019JC015756

Conferences and workshops participated in during the reported period:

Babb, D., Galley, R.J., Landy, J.C., Barber, D.G. (2020) The changing ice cover of the Beaufort Sea and the impact of recent extreme events, AGU Fall Meeting. Poster Presentation.

Tsamados, M., Holland, P., Racher, O., Heorten, H., Kimura, N., Feltham, D., Schroder, D., Stroeve, J., Ridout, A., Landy, J. (2020) Observed winter Arctic sea ice volume budget decomposition over the Cryosat-2 period, AGU Fall Meeting. Poster Presentation.

Landy, J., Bouffard, J., Wilson, C., Rynders, S., Tsamados, M., Aksenov, Y. (2020) Enhancing Arctic sea surface height and sea ice freeboard mapping with off-track leads, AGU Fall Meeting. Poster Presentation.

Heorton, H., Tsamados, M., Armitage, T., Landy, J., Ridout, A. (2020) Improved polar ocean surface wave height and surface elevation data from CryoSat-2 using a semi-analytical physical retracker, AGU Fall Meeting. Poster Presentation.

Landy, J., Bouffard, J., Wilson, C., Rynders, S., Tsamados, M., Aksenov, Y. (2020) Enhancing Arctic sea surface height and sea ice freeboard mapping with off-track leads, 2020 European Polar Science Week.

Landy, J.C. (2019) Arctic sea ice past and future: A modern era of extraordinary change, COP25 Cryosphere Pavilion Event, Madrid. Invited Oral Presentation and Panel Discussion.

Landy, J.C., Tsamados, M., Scharien, R.K., Petty, A.A., Stroeve, J.C. (2019) A Pan-Arctic kilometre-scale record of sea ice thickness and surface roughness from 2010-2019 through the application of a numerical SAR altimeter echo model to Cryosat-2, IGS Sea Ice Symposium, Winnipeg. Oral Presentation.

Landy, J.C., Tsamados, M. and Scharien, R.K. (2019) A Facet-Based Numerical Model for Simulating SAR Altimeter Echoes from Heterogeneous Sea Ice Surfaces, ESA Living Planet Symposium, Milan. Poster Presentation.

Tsamados, M., Heorten, H., Lawrence, I., Suciu, T., Ferreira, A., Fox, M., Ridout, A., de Rijke-Thomas, C., Landy, J.C. (2019) Exploring new techniques for retrieval of snow and sea ice surface characteristics, ESA Living Planet Symposium, Milan. Poster Presentation.

Tsamados, M., Petty, A., Landy, J.C., Girard-Ardhuin, F., Haas, C., Howell, S., Martin, T., Muller, J.-P., Nolin, A. W., Stroeve, J. (2019) Multi-decadal Arctic sea ice roughness, ESA Living Planet Symposium, Milan. Oral Presentation.

Landy, J.C., Komarov, A., Haas, C. and Howell, S. (2018), First observations of Arctic summer sea ice thickness from Cryosat-2. American Geophysical Union (AGU) Annual Fall Meeting, Washington D.C. U.S. Oral Presentation.

Landy, J.C., Tsamados, M. and Scharien, R.K. (2018), A new facet-based numerical model for simulating SAR altimeter echoes over heterogeneous sea ice surfaces. UK Sea Ice Group Meeting, NOC Southampton, UK. Oral Presentation.

Landy, J.C., Komarov, A., Haas, C. and Howell, S. (2018), Towards a reliable method for measuring Arctic sea ice thickness from satellite radar altimetry during summer months. International Circumpolar Remote Sensing Symposium, Potsdam, Germany. Oral Presentation. Award winner: best oral presentation at symposium.